

Bending insensitive sensors for strain and temperature measurements with Bragg gratings in Bragg fibers

Ningliang Liu,^{1,3} Yuhua Li,^{1,3} Ying Wang,² Haiyan Wang,¹ Wenbin Liang,¹
and Peixiang Lu^{1,2,*}

¹ Wuhan National Laboratory for Optoelectronics, Huazhong University of Science & Technology, Wuhan 430074, China

² School of Science, Wuhan Institute of Technology, Wuhan 430074, China

³ These authors contributed equally to this work

*lupeixiang@mail.hust.edu.cn

Abstract: A novel fiber Bragg grating (FBG) has been inscribed in all solid Bragg fiber by an infrared femtosecond laser. Temperature, strain and bending characteristics of the induced FBG are investigated experimentally. Four resonant dips in the transmission spectrum show positive sensitivity for temperature/strain and zero-sensitivity for bending in wavelength. Cross-sensitivity between strain/temperature and bending can thus be avoided since the resonant wavelengths are insensitive to curvature variation when the fiber is bent toward two opposite directions. Evident wavelength hysteresis is observed during the isochronal annealing test and it can be eliminated by a pre-annealing treatment. These proposed FBGs are very attractive candidates for multi-parameter sensors in harsh environment.

© 2011 Optical Society of America

OCIS Codes: (060.2370) Fiber optics sensors; (060.3735) Fiber Bragg gratings; (060.4005) Microstructured fibers.

References and links

1. A. D. Kersey, M. A. Davis, H. J. Patrick, M. LeBlanc, K. P. Koo, C. G. Askins, M. A. Putnam, and E. J. Friebele, "Fiber grating sensors," *J. Lightwave Technol.* **15**(8), 1442–1463 (1997).
2. O. Frazão, J. L. Santos, F. M. Araujo, and L. A. Ferreira, "Optical sensing with photonic crystal fibers," *Laser Photon. Rev.* **2**(6), 449–459 (2008).
3. C. Martelli, J. Canning, N. Grothoff, and K. Lyytikäinen, "Strain and temperature characterization of photonic crystal fiber Bragg gratings," *Opt. Lett.* **30**(14), 1785–1787 (2005).
4. O. Frazão, J. P. Carvalho, L. A. Ferreira, F. M. Araujo, and J. L. Santos, "Discrimination of strain and temperature using Bragg gratings in microstructured and standard optical fibers," *Meas. Sci. Technol.* **16**(10), 2109–2113 (2005).
5. Y. P. Wang, H. Bartelt, W. Ecke, R. Willsch, J. Kobelke, and M. Rothardt, "Sensing properties of fiber Bragg gratings in small-core Ge-doped photonic crystal fibers," *Opt. Commun.* **282**(6), 1129–1134 (2009).
6. C. Chen, A. Laronche, G. Bouwmans, L. Bigot, Y. Quiquempois, and J. Albert, "Sensitivity of photonic crystal fiber modes to temperature, strain and external refractive index," *Opt. Express* **16**(13), 9645–9653 (2008).
7. Y. Zhu, P. Shum, H.-W. Bay, M. Yan, X. Yu, J. Hu, J. Hao, and C. Lu, "Strain-insensitive and high-temperature long-period gratings inscribed in photonic crystal fiber," *Opt. Lett.* **30**(4), 367–369 (2005).
8. P. Yeh, A. Yariv, and E. Marom, "Theory of Bragg fiber," *J. Opt. Soc. Am. B* **68**(9), 1196–1201 (1978).
9. M. Yan and P. Shum, "Analysis of perturbed Bragg fibers with an extended transfer matrix method," *Opt. Express* **14**(7), 2596–2610 (2006).
10. K. J. Rowland, S. V. Afshar, and T. M. Monro, "Novel Low-Loss Bandgaps in All-Silica Bragg Fibers," *J. Lightwave Technol.* **26**(1), 43–51 (2008).
11. H. T. Bookey, S. Dasgupta, N. Bezawada, B. P. Pal, A. Sysoliatin, J. E. McCarthy, M. Salganskii, V. Khopin, and A. K. Kar, "Experimental demonstration of spectral broadening in an all-silica Bragg fiber," *Opt. Express* **17**(19), 17130–17135 (2009).
12. D. Chen, T.-J. Yang, J.-J. Wu, L. Shen, K.-L. Liao, and S. He, "Band-rejection fiber filter and fiber sensor based on a Bragg fiber of transversal resonant structure," *Opt. Express* **16**(21), 16489–16495 (2008).
13. L. Ma, T. Katagiri, and Y. Matsuura, "Surface-plasmon resonance sensor using silica-core Bragg fiber," *Opt. Lett.* **34**(7), 1069–1071 (2009).
14. O. Frazao, L. M. N. Amaral, J. M. Baptista, P. Roy, R. Jamier, and S. Fevrier, "Strain and Temperature Discrimination using Modal Interferometry in Bragg Fibers," *IEEE Photon. Technol. Lett.* **22**(21), 1616–1618 (2010).

15. M. S. Ferreira, J. M. Baptista, P. Roy, R. Jamier, S. Fevrier, and O. Frazao, "Highly birefringent photonic bandgap Bragg fiber loop mirror for simultaneous measurement of strain and temperature," *Opt. Lett.* **36**(6), 993–995 (2011).
 16. L. Jin, Z. Wang, Q. Fang, Y. G. Liu, B. Liu, G. Kai, and X. Dong, "Spectral characteristics and bend response of Bragg gratings inscribed in all-solid bandgap fibers," *Opt. Express* **15**(23), 15555–15565 (2007).
 17. C.-L. Zhao, Z. Li, M. S. Demokan, X. Yang, W. Jin, and C. Lu, "Studies on Strain and Temperature Characteristics of a Slanted Multimode Fiber Bragg Grating and Its Application in Multiwavelength Fiber Raman Ring Laser," *J. Lightwave Technol.* **24**(6), 2394–2400 (2006).
 18. D. Grobncic, C. W. Smelser, S. J. Mihailov, and R. B. Walker, "Long-term thermal stability tests at 1000°C of silica fibre Bragg gratings made with ultrafast laser radiation," *Meas. Sci. Technol.* **17**(5), 1009–1013 (2006).
 19. M. Douay, E. Fertein, W. X. Xie, P. Bernage, P. Niay, J. F. Bayon, and T. Georges, "Thermal Hysteresis of Bragg Wavelengths of Intra-core Fiber Gratings," *IEEE Photon. Technol. Lett.* **5**(11), 1331–1334 (1993).
 20. L. Jin, W. Jin, and J. Ju, "Directional Bend Sensing With a CO₂-Laser-Inscribed Long Period Grating in a Photonic Crystal Fiber," *J. Lightwave Technol.* **27**(21), 4884–4891 (2009).
-

1. Introduction

Fiber Bragg gratings (FBGs), which have the advantages of high sensitivity, high spatial resolution and wavelength division multiplexing capability, have been widely investigated as sensing elements for physical parameter measurements such as strain and temperature [1]. In the past decades, photonic crystal fibers (PCFs) have been undergoing rapid development in the fields of optical sensing [2], thus a large number of optical fiber gratings including Bragg gratings (FBGs) and long period gratings (LPGs) have been investigated in various PCFs with different inscription techniques [3-7]. Most works mentioned above have focused on the strain and temperature sensing of the fiber gratings. However, the measurement accuracy of these sensors could be further improved if the parameters to be measured can be avoided from other perturbations such as bending. In other words, cross-sensitivity between temperature/strain and bending is a limitation of such gratings used for the multi-parameter sensors since they are difficult to be eliminated. The new emerging Bragg fibers (including solid-core and hollow-core Bragg fibers) can be attributed to the photonic crystal fibers family generally and provide opportunities of constructing bend-insensitive devices [8]. Recently they have attracted significant attention because of their easiness in fabrication, convenience to be spliced with single mode fibers (SMFs) and robustness of structural degradation. To date, most of the studies about Bragg fibers have concentrated on the modal characteristics and optical losses theoretically [9,10]. Experimental demonstration of spectral broadening in an all-silica Bragg fiber was recently reported [11]. And the Bragg fibers used as band-rejection filters and fiber sensors for physical parameter measurements have been well investigated due to their interesting dispersion and unique modal properties [12-15]. However, to the best of our knowledge, there is still not the real fabrication of FBGs or FBG-based optical devices by use of Bragg fibers (especially all solid Bragg fibers) that may meet the increasing commercial demands of shape sensors.

In this paper, we report a novel wavelength-encoded sensor based on a fiber Bragg grating that written in non-photosensitive all solid Bragg fiber by use of 800 nm femtosecond laser irradiation. The spectral characteristics and sensing properties of the induced FBG have been investigated theoretically and experimentally. Four resonant dips in the transmission spectrum are observed and they present similar sensitivity for strain and different sensitivities for temperature with a red-shift. The simultaneous measurement of strain and temperature is performed by using the matrix equation method, and the strain and temperature resolutions are about $\pm 26 \mu\epsilon$ and $\pm 1.2^\circ\text{C}$. In bend sensing, the resonant wavelengths show negligible fluctuations and nearly zero-sensitivity to the curvature, and thus the cross-sensitivity between temperature/strain and bend could be avoided originally. These positive results show such gratings are very attractive sensing elements for multi-parameter sensors in the fields of health monitoring.

2. FBG fabrication and spectral characteristics

In the experiment carried out, an all solid Bragg fiber (Fiberhome Company) was used, which is composed of concentric cladding layers of alternating high and low index rings and

fabricated by Plasma Chemical Vapor Deposition (PCVD). The refractive index profile (RIP) of the Bragg fiber core-pre-form with 12mm diameter was measured by York Pre-form Analyzer P104 instrument, as shown in Fig. 1(a). A microscopic image of the fiber cut is shown in Fig. 1(b). It has a compound core including a low index dark core of 3.3- μm -diameter and a high index bright ring of 3.1- μm -thickness, of which the index difference are -0.00555 and 0.01186 to the background (shown as segment a and b in Fig. 1(a)), respectively. Total 11 periodical coaxial layers constitute the inner cladding with alternating high index rings (doped with germanium) and low index rings (doped with fluoride) based on the pure silica. The thicknesses of the innermost 6 dark rings and 5 bright rings are $2.23\ \mu\text{m}$ and $2.47\ \mu\text{m}$, respectively. And the index differences of these two types of rings to the background are -0.01540 and 0.00440 . The Bragg fiber can be easily spliced to the standard single mode fibers with a loss of approximately 2 dB. The splicing loss may be further decreased through optimizing the splicing parameters in the future. Figure 2 shows the transmission spectrum of a 2-m-long Bragg fiber in a wavelength region of 1520-1620 nm. The spectrum is recorded by use of a wideband light source (ALS-1550-20) and an Optical Spectrum Analyzer (OSA, Yokogawa AQ6370B) with a resolution of 0.02 nm. The total insertion loss is about 5 dB, as can be seen in Fig. 2. It is mainly resulted from the two splicing joints and coupling loss between light source and SMFs.

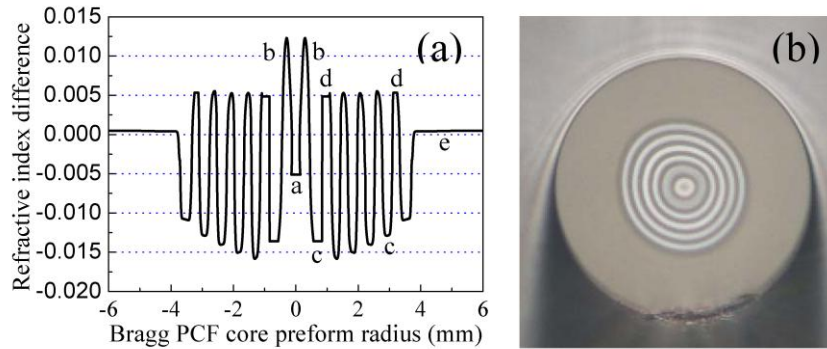


Fig. 1. The all solid Bragg fiber used in the experiments. (a) RIP of the Bragg fiber core-pre-form with 12mm diameter. (b) Microscopic photograph for the cross section of all solid Bragg fiber, the bright circles represent high refractive index area and the dark circles represent low refractive index area.

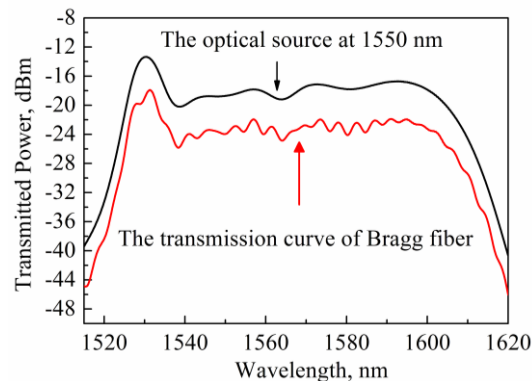


Fig. 2. Transmission spectrum measured on a 2m-long Bragg fiber by use of a wideband light source (ALS-1550-20) at 1550 nm region.

The Bragg grating was inscribed with a near-field phase mask method. Femtosecond pulses (50 fs, 1 kHz repetition rate at 800nm) were produced by a Ti: sapphire laser system

(Spectra Physics). The laser beam ($1/e$ Gaussian beam radius of about 4 mm) was focused into the fiber core through a phase mask by a cylindrical lens (focal length of 60 mm). The maximum pulse energy of the laser output was about 1.2 mJ and it can be attenuated flexibly by a half waveplate and a linear polarizer. Assuming a Gaussian light beam, the width of the focal line can be estimated to be $7.6 \mu\text{m}$. The phase mask (StockerYale) has been designed for 800 nm illumination, with the first-order diffraction efficiency of 68% and the zero-order of about 3%. The grating pitch of 3200 nm leads to the induced FBG to be a third-order grating for a wavelength at about 1545 nm. During the experiment, the fiber was located in a close distance of about 1.2 mm to the phase mask, which was accurately positioned by a high-precision three-axis translation stage. Provided that the incident beam is in Gaussian profile, a grating with a length of more than 5 mm can be obtained.

During the experiment, both ends of a 15-cm-length all solid Bragg fiber were spliced to the SMFs. FBG was written in the Bragg fiber core with the pulse energy of $650 \mu\text{J}$ and exposure time of about 60 s. Figure 3(a) shows a microscopic image of the grating fabricated in the compound core of Bragg fiber, where uniform grating fringes can be clearly observed. The transmission and reflection spectra of the induced FBG are shown in Fig. 3(b). Four deep resonant dips, marked as A (1537.72 nm, -9.22 dB), B (1541.24 nm, -13.69 dB), C (1544.63 nm, -22.66 dB) and D (1547.15 nm, -21.30 dB) can be observed in the transmission spectrum. However, only one reflection peak, marked as peak E (1547.16 nm, 11.54 dB), which corresponds to dip D, can be found in the reflection spectra. However, the reflection peaks corresponding to dip A, B and C are not observed. The possible reason is that the modes corresponding to dip A, B and C are not guided by the SMFs and result in no peaks like peak E in the reflection spectrum.

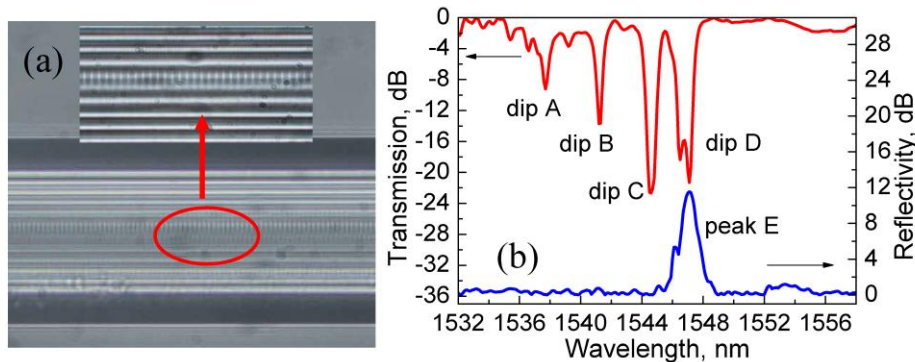
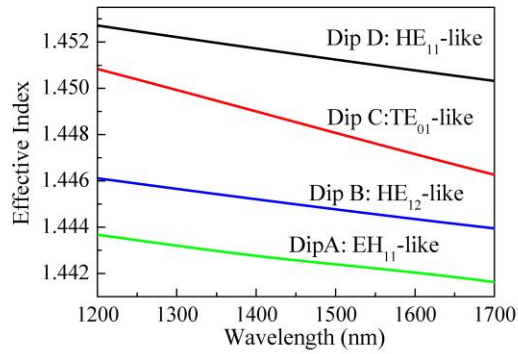
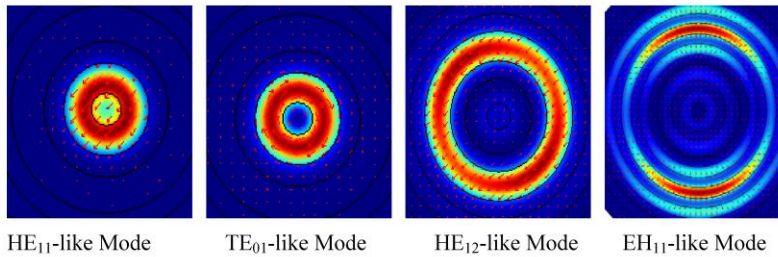


Fig. 3. (a) Microscopic image of a FBG fabricated in the all solid Bragg fiber by an 800nm femtosecond laser and a phase mask. (b) The transmission and reflection spectra of the FBG.

The all solid Bragg fiber used in this work was modeled with the geometry demonstrated in Fig. 1(b) and the materials indices are given according to the index differences in Fig. 1(a) with the silica refractive index of 1.446. Perfect matched layer was also used around the fiber. Then the dispersion properties were simulated with the Finite Element Method (FEM) to illustrate the mode coupling mechanism [16]. Four resonant modes of the Bragg fiber are confirmed to be responsible for those Bragg resonances. These modes can be labeled as HE_{11} -, TE_{01} -, HE_{21} - and EH_{11} -like mode (which correspond to dip D, C, B and A in the transmission spectrum) respectively, and their dispersion curves and modal profiles are shown in Fig. 4. The calculated effective indices around 1550 nm of these modes are in good agreement with the experimental ones. Furthermore, the numerical results confirm that the modes corresponding to dip A, B and C are not guided in SMFs, as the effective indices of EH_{11} -, HE_{12} - and TE_{01} -like modes are well below that of the fundamental mode in SMF around 1550 nm.



(a)



(b)

Fig. 4. (a) Simulated effective indices of HE_{11} -, TE_{01} -, HE_{12} -, and EH_{11} -like modes for the all solid Bragg fiber in the wavelength range from 1200 nm to 1700 nm. (b) The electric field and power distribution of these resonant modes.

Table 1. Summary of transmission resonances properties

Dip	Mode	Resonance amplitude (dB)	λ (nm)	N_{eff} (Sim)	N_{eff} (Exp)	$d\lambda/d\varepsilon$ (pm/ μE)	$d\lambda/dT$ (pm/ $^{\circ}\text{C}$)
A	HE_{11}	-9.22	1537.72	1.4423	1.4416	1.10	9.68
B	TE_{01}	-13.69	1541.24	1.4445	1.4449	1.14	10.32
C	HE_{12}	-22.66	1544.63	1.4476	1.4481	1.13	10.97
D	EH_{11}	-21.30	1547.15	1.4510	1.4504	1.12	11.20

A summary of experimental results for resonant dips A, B, C and D is given in Table 1, which exhibits quantitative details about those transmission dips, including resonant wavelength, resonant amplitude, the effective index in simulation and experiment, and the measured strain and temperature sensitivity. It can be found that, the simulated effective indices are in good agreement with the experimental ones.

3. Sensing characterization

3.1 Strain sensing

We investigate the strain sensing of the FBG inscribed in the Bragg fiber by employing an experimental setup illustrated in Fig. 5. The Bragg fiber with a FBG at its centre was hung straightforward between two high-precision translation stages. The fiber was stretched from its idle position by driving the micrometer screw of the right-hand stage along the z axis. To avoid the temperature perturbation, this experiment was carried out at a constant environment temperature of 22°C. As shown in Fig. 6(a), the resonant wavelengths of dip A, B, C and D present positive shift toward longer wavelength linearly versus strain. The sensitivities are

nearly the same (1.10 pm/ $\mu\epsilon$, 1.14 pm/ $\mu\epsilon$, 1.13 pm/ $\mu\epsilon$ and 1.12 pm/ $\mu\epsilon$ for dip A, B, C and D respectively), which are slightly higher than that of the FBG inscribed in SMF (about 1 pm/ $\mu\epsilon$) [6]. The spectral evolution of this FBG under a strain of 550 $\mu\epsilon$ and 950 $\mu\epsilon$ is shown in Fig. 6(b). It is worth to note that, the Bragg fiber exhibits comparable mechanical strength to SMF, over 5000 $\mu\epsilon$, which are stronger than that applied to most of other microstructured fibers [3-7,14,15]. It may benefit from the all solid silica structure.

The strain-induced shift of the resonant wavelength identified as $\lambda_B = 2n_{\text{eff}}\Lambda_g$ (n_{eff} is the effective refractive index and Λ_g is the grating period), is due to the photo-elastic effect and the change of grating pitch, and can be written as [5]:

$$\Delta\lambda_B = \lambda_B(1 - p_e)\epsilon_z \quad (1)$$

where ϵ_z is the tensile or compressed strain applied to the gratings, and P_e is an effective strain-optic constant. Figure 6 indicates that, the core mode resonances and cladding mode resonances have the same strain-optic tensor due to the identical silica-based material and the similar Ge-doped distribution. In other words, the effect from strain perturbation causes similar changes in effective refractive index and grating period for different modes, resulting in the four dip wavelengths vary linearly and shift with a same sensitivity [17]. This behavior is different from that of FBGs inscribed in a PCF with solid-core and air holes cladding (germanium/fluorine coped core) reported by Chen et al. [6], where different cladding modes exhibit distinctly different sensitivities to strain perturbation.

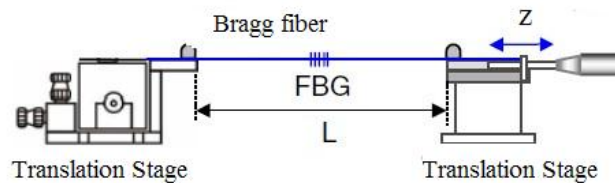


Fig. 5. Schematic of the experimental setup for strain sensing.

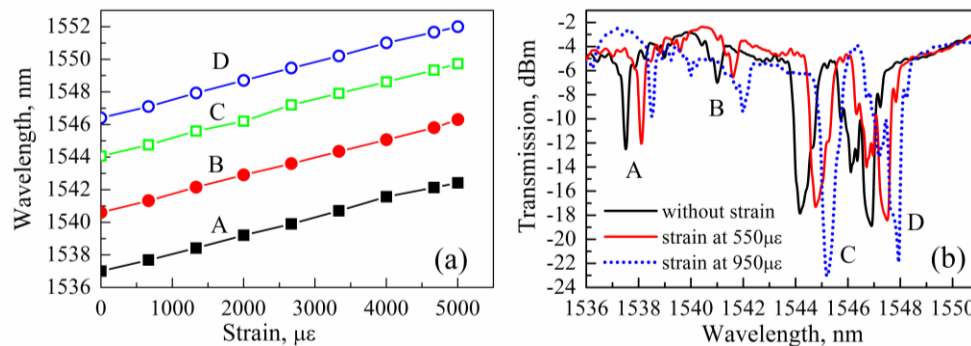


Fig. 6. (a) The resonant wavelength drifts of dip A, B, C and D with the increasing longitudinal strain. (b) The transmission spectra evolution of the FBG under different strain.

3.2 Temperature sensing

To investigate the temperature sensitivity of the induced FBG, we conducted a short-term thermal exposure, by heating the fiber from 25°C to 200°C progressively with an increment of 25°C at each step. The temperature was adjusted by an ISOTHERMAL PEGASUS^{PLUS} 1200 tube furnace that can operate from 20°C to 1200°C with a stability between $\pm 0.05^\circ\text{C}$ to $\pm 0.2^\circ\text{C}$ approximately. Figure 7(a) shows the wavelength shifts of four attenuation dips with the change of temperature. It is found that they show upward trends toward longer wavelength when temperature is increased gradually, in terms of a quadratic response. The sensitivities for the four resonant modes are approximately estimated to be 9.68 pm/ $^\circ\text{C}$, 10.32 pm/ $^\circ\text{C}$,

10.97 pm/°C and 11.20 pm/°C for dip A, B, C and D, respectively, with linear fits. The core mode has the largest sensitivity among these modes. The temperature sensitivity of the FBG we obtained is larger than that of the FBG inscribed in SMFs (about 9.6 pm/°C) [6]. No thermal hysteresis was observed when the fiber was cooled to room temperature, exhibiting a good repeatability on the second cycle of heating and cooling. Figure 7(b) shows the spectral evolution of the FBG after annealing at temperatures of 25°C, 100°C and 170°C.

The grating was also subjected to another short-time thermal exposure from 25°C to 500°C in steps of 50°C. The wavelength shifts of four dips are presented in Fig. 8(a). It is observed that the attenuation dip wavelengths have a significant hysteresis toward longer wavelength during the cooling process. For example, dip A takes a maximum hysteresis of wavelength with amplitude as high as 1.7 nm at 300°C and a red-shift of 0.5 nm is still existed when cooled down to room temperature, even after a few days. The permanent wavelength shift is also found for other dips. As well known, sensors based on FBGs used for health monitoring in harsh environments often need to be able to sustain high temperature, since the refractive index modulation (Δn_{mod}) would be annealed out at elevated temperatures and the decay of reflectivity is inevitable [18]. Thereby we studied the evolution of transmitted power of these dips by heating the fiber from room temperature to 500°C, with an increment of 50°C for 10 minutes at each stage for stabilization, and the results are shown in Fig. 8(b). Results show that four transmission dips show distinguishing responses at the beginning of annealing below 50°C, then the resonant depth began to enhance gradually until temperature was increased to 300°C, and then they began to decrease rapidly after 300°C (shown as the decay area in Fig. 8(b)). The evolution of transmitted power can be explained by the change of femtosecond-laser-induced index modulation depth, Δn_{mod} , which might increase during the initial annealing process as some unstable refractive index modulation would be erased [18]. The continuous decay of transmitted power demonstrates that FBGs inscribed in the all solid Bragg fibers cannot keep stable at temperatures higher than 300°C. This complex behavior of index modulation change may result to the wavelength hysteresis toward longer wavelength, as shown in Fig. 8(a).

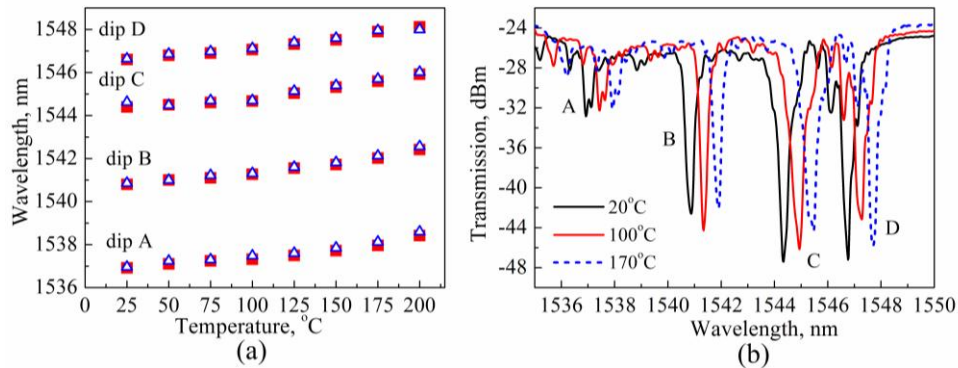


Fig. 7. (a) The resonant wavelength drifts of the FBG when subjected to a short-term thermal exposure from 25°C to 200°C (square represents heating cycle, triangle represents cooling cycle); (b) The spectral evolution of the FBG under a temperature of 25°C (black), 100°C (red) and 170°C (blue).

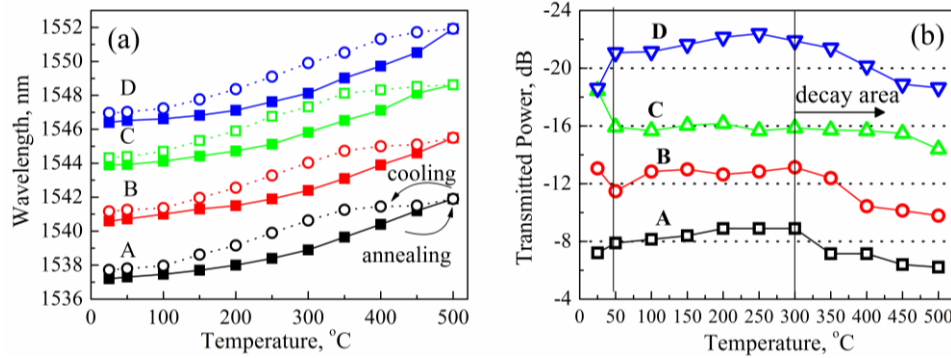


Fig. 8. (a) The resonant wavelength drifts of four dips when subjected to short-term thermal exposure from 25°C to 500°C (solid square represents heating cycle, hollow circle represents cooling cycle). (b) The evolution of transmitted power for four dips when the temperature is increased to 500°C.

The thermal response of FBG inscribed in the all solid Bragg fiber is distinguished from those linear red-shifts of FBGs inscribed in PCFs reported elsewhere [3-7,14,15]. The possible mechanism is discussed here. The temperature-induced shift of the Bragg wavelength λ_B , is due to the fiber expansion and the thermo-optic effect. It can be written as [5]:

$$\Delta\lambda_B = \lambda_B \left(\frac{1}{\Lambda} \frac{\partial\Lambda}{\partial T} + \frac{1}{n_{\text{eff}}} \frac{\partial n_{\text{eff}}}{\partial T} \right) \Delta T = \lambda_B (\alpha_\Lambda + \alpha_n) \Delta T \quad (2)$$

where ΔT is the temperature change, α_Λ is the thermal expansion coefficient for the fiber, and α_n is the thermo-optical coefficient. The λ_B is related to the effective refractive index n_{eff} and the grating period Λ_g , and both of them are temperature-dependent indeed. When the temperature increases, two Bragg wavelength-shifts of opposite signs are presented: the thermal expansion of the fiber upshifts the λ_B , meanwhile the decay in the photoinduced index variations downshifts permanently the λ_B . Generally speaking, FBGs inscribed by femtosecond laser are mainly based on a multi-photon absorption process, which can produce a local Δn_{mod} in a range from 10^{-5} to 10^{-2} [18]. When temperature is below the threshold temperature (T_g) of the fiber material, the contribution determined by the variation in n_{eff} is the dominant effect since α_Λ is very small for the Ge-doped silica-core fiber [5]. Hence, the sensitivity is dominated by the thermo-optical coefficients α_n , which is commonly not the same for different resonant modes. Thus the temperature evolution simply results in a distinct spectral shift among the four transmission dips. Recently, thermal hysteresis of wavelength depending on different inscription conditions and fiber types have been reported in the annealing of FBGs inscribed by UV laser radiation [19], and it has not been observed in those FBGs inscribed by ultrafast infrared femtosecond radiation, to the best of our knowledge. Especially for Bragg gratings, n_{eff} is determined by two factors: the refractive index of the unperturbed fiber and the index modulation depth Δn_{mod} [18]. A decay of Δn_{mod} due to grating erasure in annealing would result in a shift to shorter wavelength, which is in contrary to the experimental evidence obtained in Fig. 8(a). The dominant mechanism is still unknown; however, it is believed to be dependent with the properties of the fiber material.

The repeatability of measurement is another important feature, especially for those FBG-based wavelength-encoded sensing devices. Thereby the thermal hysteresis should be avoided experimentally to ensure the stability of output wavelength. It was proved that, the effect of wavelength hysteresis could be eliminated through a pre-annealing treatment in our experiment, by heating the FBG at 300°C for 8 hours and then increasing the temperature to 500°C again. It is believed that the long-term pre-annealing under a lower temperature can remove the thermally unstable Δn_{mod} and then a more stable Δn_{mod} could be created. Consequently, only small wavelength hysteresis of about 0.5 nm could be observed in the

cooling stage when the temperature was above 400°C, as illustrated in Fig. 9, and the hysteresis was almost negligible when the fiber was cooled down to temperatures lower than 300°C. So the repeatability of the induced FBG can be improved through the pre-annealing process. This positive result implies that such gratings are attractive sensing elements for monitoring applications where high temperature is required.

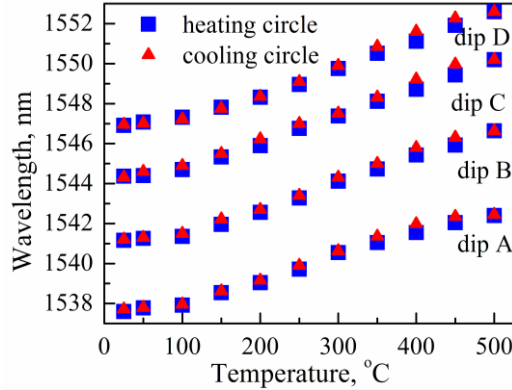


Fig. 9. The Bragg wavelength shifts of dip A, B, C and D when the temperature is cycled between 25°C and 500°C after a pre-annealing treatment at 300°C (for 8 hours) has been undertaken (blue square for heating cycle, red triangle for cooling cycle).

3.3 Simultaneous measurement of strain and temperature

In this section, we discuss the potential of such FBGs applied for the simultaneous measurement of strain and temperature. In principle, the strain and temperature perturbations can be measured simultaneously by use of the standard matrix inversion method. The matrix elements can be determined by measuring the strain and temperature sensitivities separately, and then the sensor output can be derived by the matrix equation in terms of variation in temperature at constant strain and variation in strain at constant temperature respectively [4,14,15]. The performance of the induced FBG for simultaneous measurement was determined experimentally by performing strain variations (ranging from 0 $\mu\epsilon$ to 2000 $\mu\epsilon$) at a fixed temperature (25°C) and the other way temperature variations (ranging from 25°C to 90°C) for a specific applied strain (200 $\mu\epsilon$).

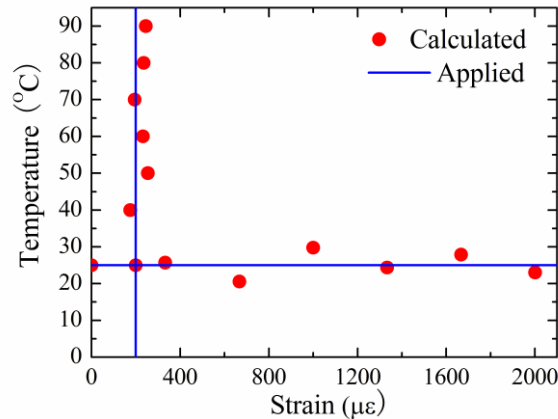


Fig. 10. Sensor output as determined by the matrix method for applied strain and temperature.

Take dip A and D for example, in view of the different strain and temperature sensitivities of them, it is feasible to measure these two parameters simultaneously using the following matrix equation [4,14,15]:

$$\begin{bmatrix} \Delta\varepsilon \\ \Delta T \end{bmatrix} = \frac{1}{M} \begin{bmatrix} K_{TD} & -K_{TA} \\ -K_{\varepsilon D} & K_{\varepsilon A} \end{bmatrix} \begin{bmatrix} \Delta\lambda_A \\ \Delta\lambda_D \end{bmatrix} \quad (3)$$

where $M = K_{\varepsilon A}K_{TD} - K_{TA}K_{\varepsilon D}$ is the matrix determinant and $K_{\varepsilon A}$, K_{TA} , $K_{\varepsilon D}$, K_{TD} is the sensitivity of dip A, D to strain and temperature respectively. From the separate strain and temperature measurements given in section 3.1 and section 3.2, the two equations for wavelength drift of dip A and D can be obtained:

$$\Delta\lambda_A = 1.1\Delta\varepsilon + 9.68\Delta T \quad (4)$$

$$\Delta\lambda_D = 1.12\Delta\varepsilon + 11.2\Delta T \quad (5)$$

Thereby according to Eq. (3), the variation of strain ($\Delta\varepsilon$) and temperature (ΔT) can be determined by the measured Bragg wavelength shifts ($\Delta\lambda_A, \Delta\lambda_D$) from the matrix:

$$\begin{bmatrix} \Delta\varepsilon \\ \Delta T \end{bmatrix} = \frac{1}{1.4784} \begin{bmatrix} 11.2 & -9.68 \\ -1.12 & 1.1 \end{bmatrix} \begin{bmatrix} \Delta\lambda_A \\ \Delta\lambda_D \end{bmatrix} \quad (6)$$

As a result, the capability of the FBG-based sensor for simultaneous measurement of strain and temperature is shown in Fig. 10. It is found that the sensor output calculated with Eq. (6) is in good agreement with the measured values applied in the experiment. The strain and temperature resolution can be estimated to be about $\pm 26 \mu\varepsilon$ and $\pm 1.2^\circ\text{C}$ since the resolution of the OSA we used is 0.02 nm.

3.4 Bend sensing

For accuracy in measurement, two different experimental setups for bend sensing were designed as described in Fig. 11: (1) Investigating microbend responses of such FBG under a small curvature from 0 m^{-1} to 20 m^{-1} using the system in Fig. 11(a). We rotated the right-hand stage's micrometer screw along the fiber axis, which resulted in a bend that lay in the vertical plane uniformly. The curvature of bend C is given by $C = 1/R = 2H/(H^2 + L^2/4)$, where H is the displacement from the straight position and L is the length of bend section. (2) Investigating sharp bend responses of the FBG under a wide curvature from 20 m^{-1} to 100 m^{-1} by making one loop at the middle of the fiber around cylindrical rods with various radius of R. The curvature C is directly dependent upon $1/R$ and the system is demonstrated in Fig. 11(b). In order to study the directional bend sensing function, the fiber was bent into two opposite orientations by the rotation stage: toward and against the femtosecond radiation exposure side, which marked as $-$ and $+$ orientation in the following results. Figure 12(a) shows the peak wavelength shifts for four dipoles versus the bend curvature ranging from -100 m^{-1} to $+100 \text{ m}^{-1}$. It is indicated that, there was no significant redshift or blueshift with the curvature variation for all of them, which is totally different from the simulated or experimental results reported by other groups previously [5,16,20]. The irregular fluctuations of wavelength along with the bend perturbation are almost within hundreds of picometers and it can be neglected since the length of grating induced in this work is more than 5mm and the radius of bend is as sharp as 1cm. Figure 12(b) shows the measured transmission spectrum of the FBG when the fiber was without bending, bent with radius of -50 cm and $+50 \text{ cm}$ respectively. There was no shift of peak wavelength but their depth became deeper or shallower. This figure clearly demonstrates the wavelength is almost not sensitive to the curvature change, also regardless of bend direction.

Generally speaking, when a symmetric or well-written FBG is bent toward opposite orientations in the diametric plane, the centre of the mode field will be subjected to an expansive strain or compressive strain, consequently the Bragg wavelength moves to shorter or longer wavelength correspondingly [5]. However, the practical centre of mode field usually does not locate within the diametric plane including the bend direction, due to an original asymmetry of fiber structure which may result from mechanical perturbations, lateral

pressures, and environment changes during the fiber fabrication. So the bending responses of resonant wavelength for different bend orientations could be not identical, probably depending on the modification of the actual fiber or FBG [5,16,20]. Here, we consider the asymmetry index modulation caused by the side-writing method of femtosecond irradiation and the geometrical asymmetry of fiber structure deformation as two of major causes responsible for the unique bending properties in this work. Besides, the influence from bending is different for cladding modes because of their differences in the modal cross-section profiles. So there will be a complicated change in the spectral profile whose mechanism is still unclear [16,20]. This bending-insensitive FBG has a great potential for temperature or strain sensing, since the cross-sensitivity between temperature/strain and bending can be well avoided, especially for those smart structures and complex devices.

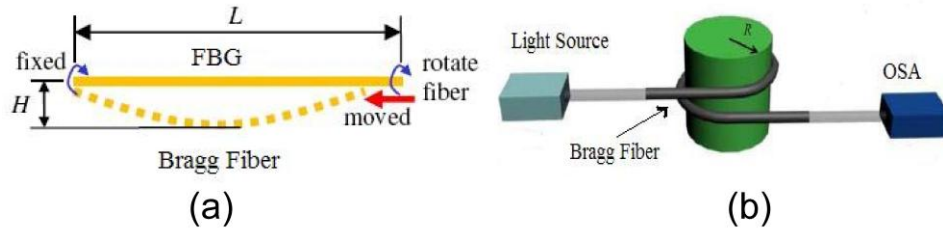


Fig. 11. Schematic of the experimental setups for the bending features of FBG fabricated in the Bragg fiber. (a) Designed for curvature from 0 m^{-1} to 20 m^{-1} , (b) Designed for curvature from 20 m^{-1} to 100 m^{-1} .

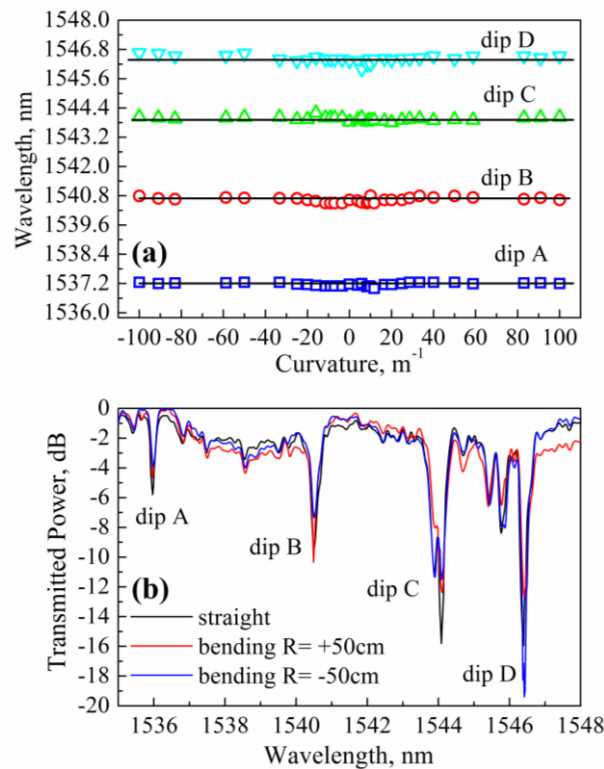


Fig. 12. (a) The evolution of location of peak wavelength for four dips with the curvature from -100 m^{-1} to $+100 \text{ m}^{-1}$. (b) The evolution of transmission spectra of the induced FBG in Bragg fiber under different bend radiuses.

4. Conclusion

In conclusion, we propose a novel wavelength-encoded sensor based on Bragg gratings written in non-hydrogenated all solid Bragg fibers by femtosecond laser irradiation. The spectral properties and sensing characterizations of this FBG have been investigated in detail. Four obvious transmission dips of the induced FBG present similar sensitivity for strain and different sensitivities for temperature with a positive shift toward longer wavelength. Meanwhile, it shows wavelength-independence to the variation of curvature and bend direction. The simultaneous measurement of temperature and strain has also been undertaken by using matrix equation method, which indicates the feasibility to be used in the functionality of multi-parameter measurements. Thermal hysteresis toward longer wavelength during the short-term annealing test could be eliminated by use of a pre-annealing treatment, and the FBG after pre-annealing would sustain a temperature of more than 500°C with a good repeatability. These advantages make such proposed FBGs that fabricated in all solid Bragg fibers serve as ideal candidates for multi-parameter sensors, especially suitable for health monitoring in harsh environments.

Acknowledgments

This work was supported by National Natural Science Foundation of China under Grant No. 61008013 and No.60925021, and the Fundamental Research Funds for the Central Universities under HUST: HF-07-12-2010-230.